Article

A Versatile Analog Electronic Interface for Piezoelectric Sensors Used for Impacts Detection and Positioning in Structural Health Monitoring (SHM) Systems

Lorenzo Capineri *(ID) and Andrea Bulletti (ID)

Department of Information Engineering, University of Florence, 50139 Florence, Italy; andrea.bulletti@unifi.it
* Correspondence: lorenzo.capineri@unifi.it

Abstract: Continuous monitoring of mechanical impacts is one of the goals of modern SHM systems using a sensor network installed on a structure. For the evaluation of the impact position, there are generally applied triangulation techniques based on the estimation of the differential time of arrival (DToA). The signals generated by impacts are multimodal, dispersive Lamb waves propagating in the plate-like structure. Symmetrical S_0 and antisymmetrical A_0 Lamb waves are both generated by impact events with different velocities and energies. The discrimination of these two modes is an advantage for impact positioning and characterization. The faster S_0 is less influenced by multiple path signal overlapping and is also less dispersive, but its amplitude is generally 40–80 dB lower than the amplitude of the A_0 mode. The latter has an amplitude related to the impact energy, while S_0 amplitude is related to the impact velocity and has higher frequency spectral content. For these reasons, the analog front-end (AFE) design is crucial to preserve the information of the impact event, and at the same time, the overall signal chain must be optimized. Large dynamic range ADCs with high resolution (at least 12-bit) are generally required for processing these signals to retrieve the DToA information found in the full signal spectrum, typically from 20 kHz to 500 kHz. A solution explored in this work is the design of a versatile analog front-end capable of matching the different types of piezoelectric sensors used for impact monitoring (piezoceramic, piezocomposite or piezopolymer) in a sensor node. The analog front-end interface has a programmable attenuator and three selectable configurations with different gain and bandwidth to optimize the signal-to-noise ratio and distortion of the selected Lamb wave mode. This interface is realized as a module compatible with the I/O of a 16 channels real-time electronic system for SHM previously developed by the authors. High-frequency components up to 270 kHz and lower-frequency components of the received signals are separated by different channels and generate high signal-to-noise ratio signals that can be easily treated by digital signal processing using a single central unit board with ADC and FPGA.

Keywords: impact monitoring; electronic front-end; analog signal processing; structural health monitoring

1. Introduction

Continuous impact monitoring systems have the purpose of detecting events capable of generating damage to critical structures or components and therefore have an interest in the SHM field [1–6]. These systems are rapidly evolving to meet the needs of the aerospace, automotive, and energy conversion and transportation industries [7–9]; the evolution consists in transforming the electronic laboratory systems towards distributed architectures of autonomous sensor nodes installed on the structure to be monitored [10].

Impacting objects can have different mass and speed and therefore different energy, in addition to different shapes and sizes, and so are difficult to predict and model.

The event of an impact can be detected and characterized by different types of sensors, such as piezoelectric sensors for the detection of guided ultrasonic waves [11–15] or stress/deformation through optoelectronic sensors, such as Fiber Bragg Gratings [16–19] and others. Obviously, each type of sensor needs an appropriate electronic front-end.

This work addresses the problems related to the study of a new architecture for the analog front-end that can be used in a sensor node. The characteristics of this electronic interface are fully exploited to reduce the sampling frequency and resolution of the analog-to-digital converter and reduce the capabilities of the computational resources for the pre-processing of the signal generated by an impact. In this regard, various solutions are reported in the literature with an analysis of different circuit architectures for interfacing piezoelectric sensors [20–22].

In this article, the main characteristics of signals captured with piezoelectric sensors for ultrasound-guided waves (UGW) are described in Section 1; this physical information is important for the electronic project because it allows the quantitative definition of the main parameters for the multichannel electronic interface that can be used in a versatile way for different signal processing and different sensor characteristics (impedance, band).

Section 2 defines the requirements of the design for the extraction of different information from the signal generated by an impact, and some comparative considerations are made concerning the analog interface AFE with respect to a digital solution for acquisition and processing.

Section 3 describes the hardware design and construction of a programmable AFE module for use with different types of piezoelectric sensors to be inserted in a 16-channel acquisition system [23,24] for structural health monitoring. Finally, Section 4 reports the experimental results obtained by different impacts on an aluminum plate. The conclusions discuss the advantages of the proposed solution for an AFE integrated with an autonomous sensor node.

As previously discussed, the problem with the design of the AFE is that of choosing the type of piezoelectric sensor and the analog processing chain capable of extracting useful information for the application of triangulation algorithms for estimating the position of the impact [25–28] and for the determination of energy to assess any damage and prognostics [6,15].

The useful information contained in the ultrasonic-guided waves is the differential arrival times between different sensors and the energy of the impact. The literature reports various methods for estimating DTOAs by means of the early arrival signal that has propagated from the unknown impact point to the known position of one of the sensors installed on the structure. Since the ultrasound-guided waves in a laminar structure are multimodal-dispersive Lamb waves [29] with well-defined frequency dependent attenuation [30], it is necessary to be able to robustly extract the first arrival signal from the background noise. At the same time, the signals from highly energetic impacts (e.g. >1 Joule) can have amplitudes that saturate the dynamics of the first stage, notably limited by the available supply voltage rail. Moreover, the phenomenon of saturation prevents the extraction of information on energy, and the need for a recovery time during which the system is unavailable for recording subsequent impacts. From these considerations, it is clear how the choice of AFE electronics is important to optimize the performance of a modular system for SHM [31,32].

In Figure 1 (top), the main elements involved in the on-site SHM system for impact monitoring are illustrated. It is important to notice the strong influence of the environmental factors (temperature, pressure, dust, humidity, ice, etc.) on the sensor nodes and the propagation of ultrasonic-guided waves. The operability of electronics in harsh environments is a challenging topic but is beyond the scope of this paper. In Figure 1 (bottom), the main electronic components of a node are described. The node architecture is an important topic of research; the interested reader can find in [33] an example of advanced systems that fully exploit the MEMS technology. The design solutions for power saving using continuous impact monitoring electronics are another important task to be solved in completing the electronic design. The main work on this topic is published in the literature [34,35]. The work presented here focuses on the analog front-end design.
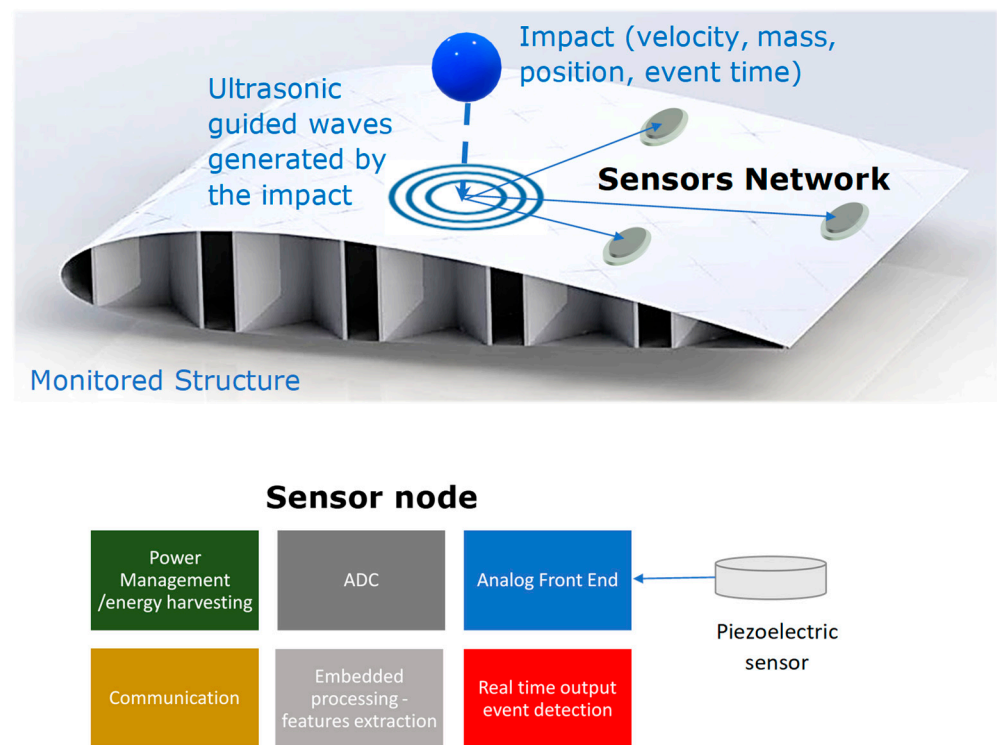
Figure 1. (**Top**) Graphical description of a continuous impact monitoring system based on a network of piezoelectric sensor nodes. (**Bottom**) Electronic blocks for a sensor node.

2. Characteristics of Impact Signals for the Design of an Electronic Front-End

In this section, we will describe the main physical relationships for a body that impact the plate-like structure and the characteristics of the generated ultrasonic-guided waves. The starting point is to collect data for the different types of impacts that must be detected and processed by an electronic module connected to a piezoelectric sensor.

2.1. Impact Energy and Propagation Velocity of Ultrasonic Guided Waves

Here we recall the main relationships for the characterization of an impact event, and later in this section, the conversion from mechanical energy into the propagation of energy by ultrasonic guided waves. A body of mass m falling from a height h, the potential energy U and the equivalent kinetic energy E_k result:

$$U = mgh \text{ [J]} \tag{1}$$

$$E_k = 1/2mv^2 \text{ [J]} \tag{2}$$

where g is the acceleration due to gravity.

Neglecting the friction with the air, the relationship between height and final speed v_f can be derived from (2):

$$v_f = \sqrt{2gh} \left[\frac{m}{s}\right] \tag{3}$$

It is interesting to remember how the conversion of the energy of the impacting body can be converted into the propagation energy of the guided waves by means of a dynamic contact between two bodies. The analysis of this complex mechanical problem was made by Hertz, who studied the conditions for having the Hertzian contact between two elastic solids [36].

In 1969, a study by C. Jackson and S. Yang [37] was published, based on Hertz's studies, to validate their theories even in dynamic conditions. The result is that, in addition to the factors identified by Hertz to describe the laws of contact, the most relevant factor in

the case of dynamic contacts is the speed of the impacting body, assuming that the other is motionless and of significantly greater mass than the first.

In subsequent studies, the propagation speed of the energy carried by the Lamb waves was also discussed in [38,39] where authors present the theoretical study of the energy propagation speed, carried by the guided propagation waves, in non-absorbent materials, coming to affirm that the group velocity of the energy and signal coincide. Reference [40] reported the theory and the methods for estimating the efficiency of the energy conversion for the S_0 and A_0 modes.

A starting point for our analysis is the calculation of the phase and group velocity of a metal plate. The calculation can be easily performed using the GMM calculator of the LAMB MATLAB®toolbox: the instrument requests the dimensions of the laminar material, the mechanical characteristics of the material plate and of the medium with which the laminate under examination is immersed.

The phase and group velocities of symmetrical (extensional) and antisymmetric Lamb waves (flexural) are therefore given as a function of frequency. The solution of Lamb's equations is shown as an example, for the phase velocity and the group velocity (see Figure 2), using a homogeneous aluminum plate, 1.4 mm thick, with air on both sides, in a simulation. In the simulation, higher-order modes are not considered, and an infinite surface of the plate is assumed, therefore neglecting boundary effects. Finally, is worth noticing that in the low-frequency region (e.g. below 500 kHz), the A_0 mode is dispersive, while the S_0 mode has an almost constant phase velocity. This observation will be recalled later as relevant for the design of the AFE electronics.
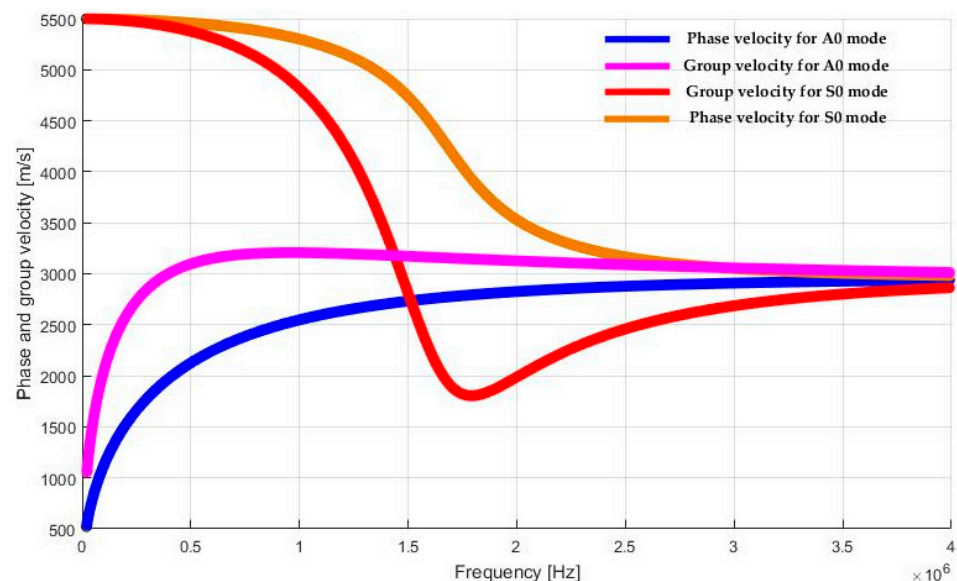
Figure 2. Dispersion curves of the group velocity (bottom) and phase velocity (top) of the 0 order modes of Lamb waves in a homogeneous aluminum plate with thickness 1.4 mm.

2.2. Analysis of Spectral Content of Lamb Wave Modes Generated by Impacts

B.C. Lee and W.J. Staszewski show in [38,41] how a wave in guided propagation within a material maintains its band, so the frequencies associated with the signal components with the greatest energy can be profitably utilized through the use of piezoelectric sensors fixed on the structure under examination.

For the verification of this characteristic property of high-speed impacts, in the document [42], the analysis of the signals obtained with the following experiment are reported: the impacts of 4.5 mm diameter spheres are fired with a compressed air pistol (Daisy model 880) on an aluminum plate, inclined 90° with respect to the plate.

The final speed of the impact is equal to 210 m/s, corresponding to a kinetic energy equal to 8.2 J. Generally, this range of speed and energy is not used in laboratory experi-

ments because it can damage the structure, while it can be used for final test of technological demonstrators. The sensors used by Digital Wave Corp., model B1025, are small to avoid distortion effects due to phase cancellation for higher frequency components (up to 1 MHz). The signals were acquired directly using a 12-bit LeCroy Model 6810 oscilloscope, at a sampling rate of 2 MHz. The sensors were positioned 15.2 cm away from impact. From the analysis reported in [42], two modes of order 0 can be distinguished (see Figure 3), a slower one, namely flexural mode, or A_0, and a faster one, extensional mode or S_0.
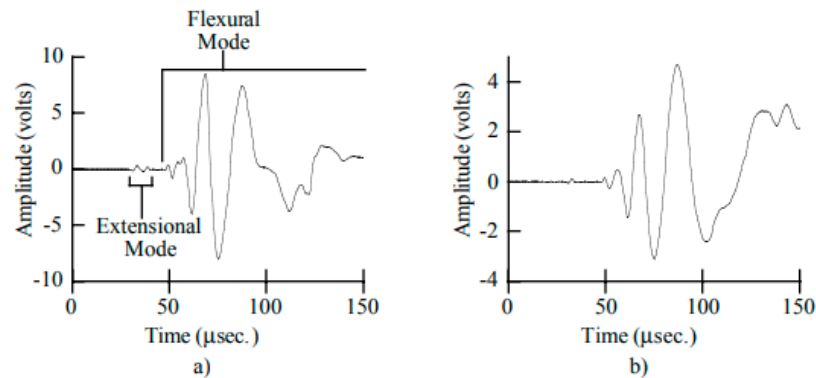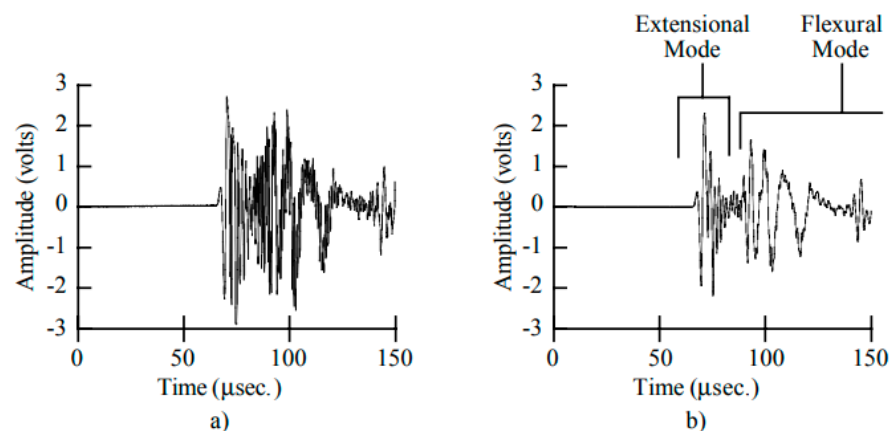

Figure 3. Signals generated by low-velocity impacts: (**a**) generated by a 5-times loaded compressed-air gun, (**b**) generated by a 2-times loaded compressed air gun [42].

We can observe that the A_0 is the dominant mode while the detection of the S_0 mode is greater than the speed of the bullet. The study then moved on to high-speed impacts, up to 700 m/s, generated by nylon bullets from air rifles, Swift 5.59-mm caliber rifle, with a 90° incident angle.

The signal is filtered by a low pass filter at the cut-off frequency of 800 kHz, to eliminate the higher order modes not considered in this analysis (see Figure 4). The prevailing mode becomes the S_0, which exceeds the A_0 mode amplitude, and its duration is also significantly increased. Summarizing from this study the relationship between impact speed and propagation mode in an aluminum plate is highlighted; the factors that depend on the impact speed are:

- the amplitude of the signal;
- the portion of the spectrum occupied (faster impacts correspond to higher frequencies);
- the presence, amplitude and duration of the S_0 mode.

Figure 4. Signals generated from a high-velocity impact: (**a**) original signal without filtering, (**b**) same signal after 800 kHz low-pass filtering [42].

2.3. Impact Localization by Triangulation Methods

Among the various possible ways to detect the position of the emission source of Lamb's guided waves, the triangulation method requires post-processing that uses fewer resources than other methods, based, for example, on Continuous Wavelet Transform (CWT) [43–45].

The triangulation method is based on the measurement of the DToAs [27,46,47], among the various sensors, and the phase velocity of these signals that in general have different paths. The calculation criterion of the DToA is not unique, and the velocity estimate affects the precision and accuracy of the localization results.

To elaborate a more reliable criterion, knowledge of the phenomena under examination is necessary: in particular, the factors that condition the signals related to the generated Lamb waves [36,37].

Furthermore, is important to understand the propagation of energy transported by Lamb waves [39] and the conservation of the frequencies associated with these energies during the path of signals through materials are known [48] as they need to be correctly acquired by the electronics for post-processing algorithms.

In the studies carried out on the modalities of triangulation of the impacts [46,49,50], it is clear that the use of the S_0 mode is preferable to the use of the A_0 mode, as it is moderately subjected to the problem of dispersion up to 1 MHz (see Figure 2), and consequently it is possible to use algorithms that require a reduced post-processing for the calculation of the DToA, and therefore of the impact position [50]. This perspective is interesting considering the advanced sensor nodes (see Figure 1) with embedded processing capabilities [12,26].

Algorithms that use A_0 mode, being present even at low impact speeds, require more processing [25,46,49]. Furthermore, the S_0 mode has a greater attenuation of the A_0 mode at low frequencies, as shown in the viewgraphs in Figure 5; this simulation reports the calculation of the imaginary part of the wave number k of the propagating wave, according to Lamb wave mode theory [29,51]. Therefore, the processing chain will have to foresee a filtering for the extraction of the S_0 signal, which has an amplitude lower than the A_0 mode.
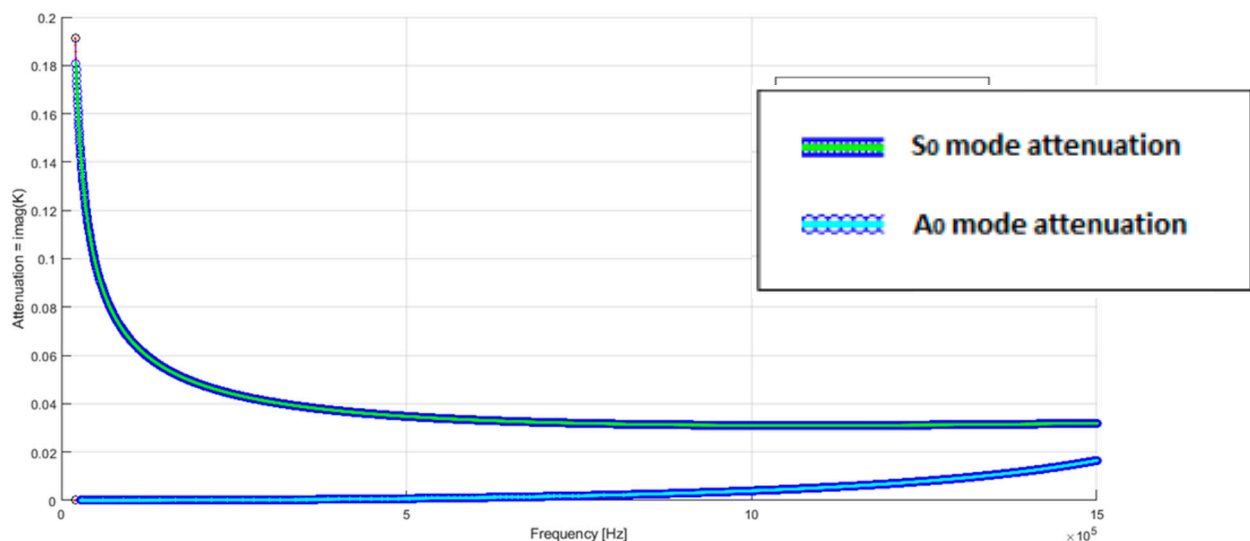
Figure 5. Simulation of the attenuation of the order S_0 and A_0 modes of the Lamb waves for a 1.4 mm thick aluminum laminate.

2.4. Characterization of the A_0 Mode Signal for Low Energy—Low Velocity Impacts

The validation of this theory has been done by an experimental session, by generating impacts with different potential energy U and different final velocities. This experiment well represents a common laboratory set-up for non-destructive impacts on metal and composite materials plate like structures. The signals have been recorded by two different

piezoelectric sensors: a PI model 876.SP1 and a custom made circular PVDF sensor. The two sensors are shown in Figure 6 and the main characteristics are reported in Table 1. The two sensors are placed at the same distance equal to 10 cm from the impact point.
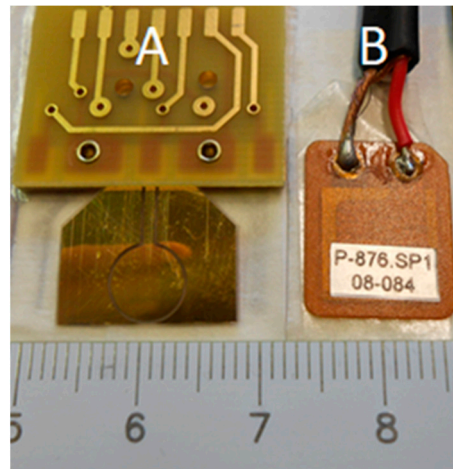
Figure 6. Example of two different type of piezoelectric sensor for SHM: (**A**) circular PVDF sensor made with bioriented PVDF film furnished by Precision Acoustics, (**B**) Piezocomposite, model DuraAct produced by Physik Instrumente. At the bottom, the ruler tick is 1 mm.

Table 1. Characteristics of sensors.

Type	A	B
Model	Circular_PVDF	P-876.SP1 DuraAct
Manufacturer	By authors [25] (Precision Acoustics material)	Physik Instrumente
Capacitance	86pF	8 nF +/−20%
Thickness piezoelectric element (μm)	110	200
Material	Piezo-polymer	Piezo-ceramic
Shape	Circular	Rectangular
Dimensions (mm)	6	16×13
Operation temperature range	−80 °C, +50 °C	−20 °C, +150 °C

The results of this experiment are summarized in Table 2. The peak voltage corresponds to the first arrival A_0 mode signal amplitude, while the S_0 is not detectable, as predicted by theory for low energy/low velocity impact. As for the band of the measured signals, the Welch method was used to estimate of the power spectral density (PSD), which contains 99% of the signal energy: for the signals under consideration, this band is contained in [0–18 kHz], that is the audible band, as expected based on Ross's studies [50]. The other consideration is about the different sensitivity of the two sensors: the piezoceramic sensor PI has a sensitivity about 20 times greater than the PVDF, and the highest voltage amplitude is 9.09 V. Such large amplitude is capable to deeply saturate a first stage of an electronic chain supplied by low voltages (e.g. 5 V or 3.3 V). Finally, we observe that the series of voltage amplitudes (columns "a"-"e" in Table 2) are almost proportional to the potential energy U while are not well correlated with impact final velocity v_f.

Table 2. Peak voltages recorded with PI.876.SP1 and PVDF the sensors with varying test mass m and free-fall height h.

	A	b	c	d	e
h (m)	0.1	0.2	0.5	0.5	0.5
mass (g)	2	2	2	4.7	8.7
U (mJ)	1,96	3.92	9.81	23	42
Vf (m/s)	1.4	1.98	3.13	3.13	3.13
Vpeak PI (V)	3.8	5.06	7.9	8.3	9.09
Vpeak PVDF (V)	0.158	0.201	0.27	0.31	0.28

In summary, the detection of an impact event by A_0 mode and the estimation of its energy by signal chain is rather simple, and the only concern is to avoid the saturation of electronics by using a programmable attenuator and a clipping circuit. The bandwidth is almost all in the audible frequency range. For energetic impacts (greater than 1 J), sensors with low sensitivity can be adopted.

2.5. Extraction of the S_0 Mode Signal by High-Pass Signal Filtering for the DToA Estimation

For this study, an impact generated by an 8.7 g sphere in free-fall from 50 cm was generated with an impact velocity of 3.13 m/s (see data in column "e" of Table 2). The impact signal was detected with a PI sensor at 10 cm from the point of impact and was acquired through an oscilloscope. The study was limited to the first 400 µs of the acquisition trace, because after this acquisition window, the signal begins to be affected by the bounces at the boundaries. The signal was acquired with a Tektronix MDO3104 digital oscilloscope with a resolution of 12 bits and bandwidth limited to 20 MHz; the full-scale voltage was adjusted to 15 V peak-to-peak to avoid saturation, and consequently the minimum distinguishable voltage is equal to 7.3 mV. Obviously, for single impact events, no averaging is possible. The original acquired single impact signal is shown in top Figure 7.
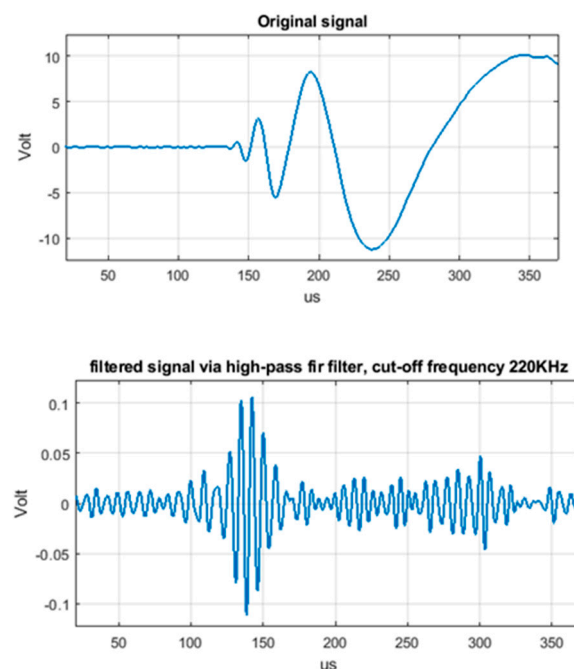
Figure 7. (**Top**) Original signal; (**Bottom**) high pass digitally FIR filter with cut-off frequency 220 kHz.

This signal has been digitally filtered with a high-pass FIR filter bank with a progressively increasing cut-off frequency from 20 kHz to 300 kHz with steps of 20 kHz. We found that with the increasing cut-off frequency, the A0 mode signal was always detectable with

reduced duration, and at 220 kHz the amplitude was still above the background noise (see bottom Figure 7).

In summary, we have demonstrated that the high-frequency components of the A0 signal can be extracted by a selective high pass digital filter applied to a sampled signal with 12-bits, but this solution is not sufficient to extract the S0 mode high-frequency components. For the sensor node design, the application of FIR digital filters on signals acquired with 12-bit resolution requires quite a lot of computational resources and transfer rate, resulting in a complex and power-demanding electronic design.

For the above reason, we decided to adopt a more classic and simple analog solution for the high pass filtering by applying a Sallen-Key active filter (gain 29 dB) with a cut-off frequency of 270 kHz. We decided to increase the cut-off frequency from 220 kHz to 270 kHz to increase the rejection of the most energetic low frequency components of the A_0 mode. The choice of this filter of 2nd order is dictated by the excellent linear phase characteristics that is fundamental for preserving the information contained by the impact signals. For the estimation of the DToA, an experimental set up is devised, as illustrated in Figure 8.
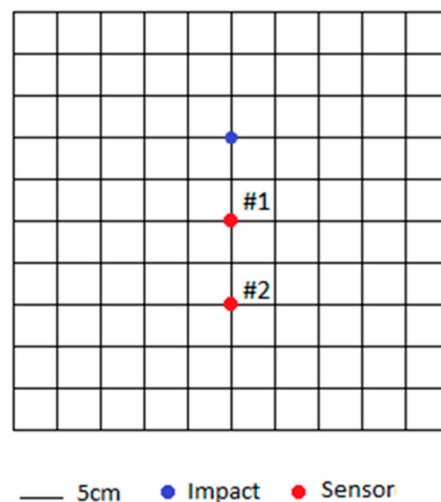

Figure 8. Experimental setup for DToA estimation by S_0 and A_0 mode signals. PI-976.SP1 piezoelectric sensors #1 and #2 are at 10 cm distance and 10 cm and 20 cm respect to the impact point (blue dot). The aluminum plate dimensions are: 500 mm × 500 mm × 1.4 mm.

The impact experiment was carried out with a sphere m = 2 g mass and free-falling height h = 50 cm (see column "c" in Table 2) to consider the worst case with lower energy impact. In Figure 9, the analog filtered normalized signals acquired by sensors #1 and #2 are shown. From these data, it is possible to extract the information of the DToA by the large amplitude A_0 mode pair assuming the arrival time of the first peak: two markers show the arrival times and the corresponding DToA is 32.65 μs, and the group velocity of 3628 m/s for a distance 10 cm. This value is in good agreement with theoretical values for the A0 mode in the high-frequency range, as reported in Figure 2.

More interestingly, in Figure 9, the other two early signals can be observed well separated from the A_0 mode signals. For the interpretation of these two signals as S_0 mode, we proceed with the analysis with DToA. A zoom of Figure 9 is useful for the analysis of the DToA as reported in Figure 10.

To verify that the observed signals represent components of the S_0 modes, we estimated the DToA equal to 19.25 μs, corresponding to a group velocity equal to 5190 m/s.

Again, this value is in good agreement with theoretical values for the S_0 mode in the high-frequency range, as reported in Figure 2. In the later part of these two signals, we can observe more remarkable differences due to dispersive characteristics.
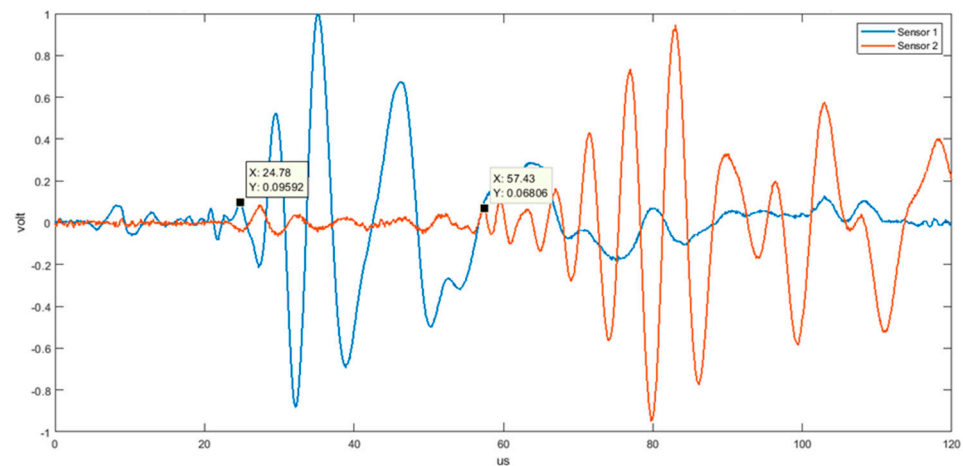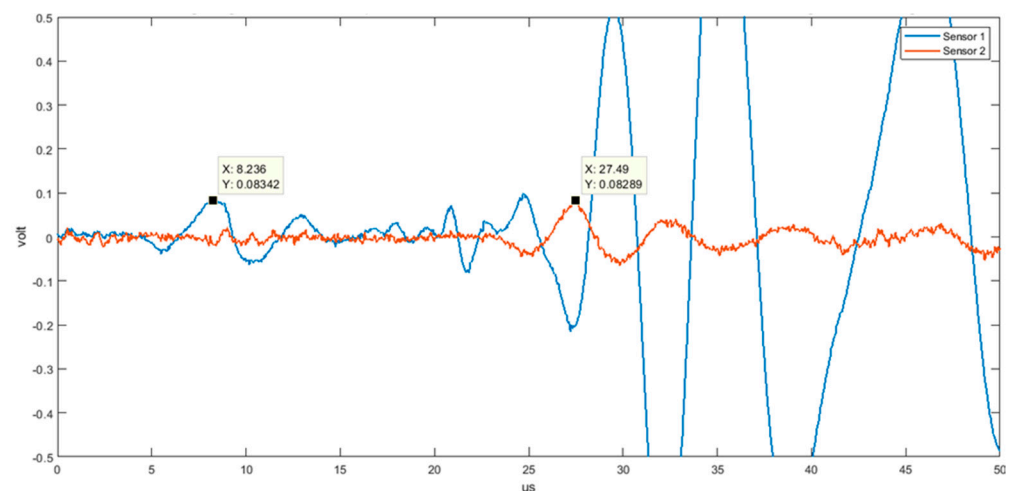
Figure 9. Impact generated signals with a sphere on an aluminum laminate and detected at 10 cm and 20 cm distance from the impact point with PI sensors—analog filtered signals.


Figure 10. Zoom of Figure 9 on a 50 µs time window for the S_0 mode signals.

It can therefore be concluded that these components belong to mode S_0 and the analog filter with cut-off frequency designed by theoretical and experimental analysis can detect the low amplitude and fast S_0 mode.

3. Design Requirements of the Receiving Electronics

This paragraph will illustrate the main requirements for AFE and the architecture of the receiving module with three different selectable and programmable measurement chains. The system must be suitable for acquiring and processing impact signals with the characteristics analyzed in the previous paragraphs. These signals can be generated either with spheres in free-fall from a height of 50 cm or an electromechanical impactor [29]. The latter can be programmed for low impact energy as Ek = 0.35 mJ and vf = 0.15 m/s; in this condition, the AFE must be able to manage signals of maximum amplitude, ranging from 9.5 Vp-p for PI sensors to 300 mVpp for PVDF sensors and a large (e.g., 300 kHz) bandwidth to avoid signal distortion. The front-end must be able to acquire both the signals for detection and energy evaluation purposes. For the DTOAs estimations, the extraction of the high-frequency components of the A_0 and S_0 modes needs dedicated channels with high pass filtering and high gain. As regards the output characteristics of the module, the connection to a multichannel acquisition system [23,24] is taken into account, with input impedance equal to 50 Ω and with 12-bit ADC dynamics equal to 1V peak-to-peak.

Figure 11 shows the block diagram of the AFE module. At the input common to all the measurement chains, there is an adjustable attenuator, followed by a buffer that separates the sensor from the rest of the processing chain and protects the subsequent stages from excessive voltages that would inevitably lead to saturation.
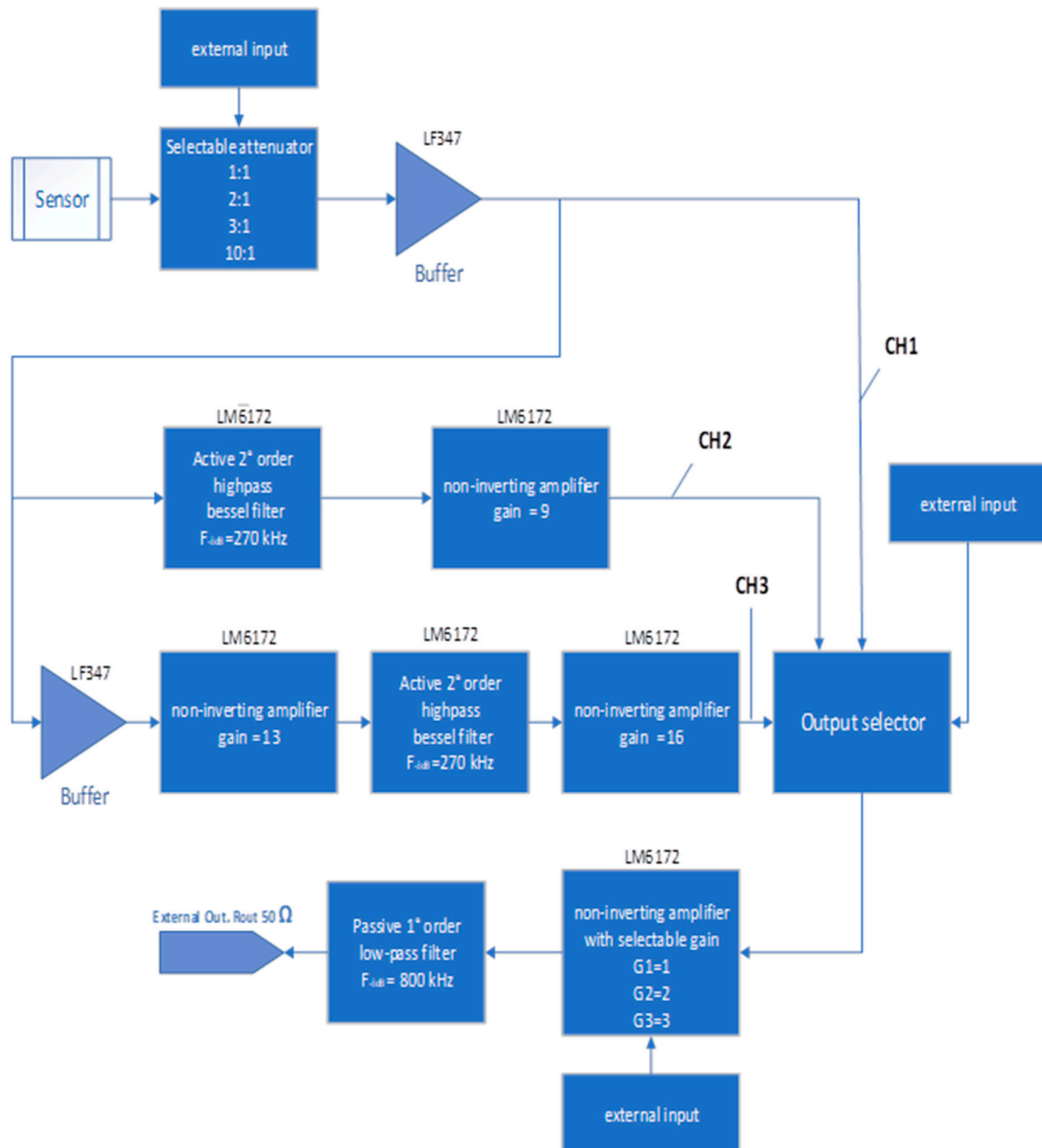
Figure 11. Block diagram of the multi-functional analog front-end. External inputs are digitally controlled from a central unit.

At the common output of the three chains, we have the programmable channel selector and a processing chain composed of a non-inverting amplifier, a low-pass filter to limit broadband noise up to 800 kHz, capable of driving a 50 Ω input impedance ADC stage.

We now describe the three different processing chains (CH1, CH2, CH3) that can be selected on each single module.

CH1 is the channel for the acquisition of raw signals: the signal acquired by the sensor passes through the attenuator, with programmable attenuation (default 10:1), then through the output selector and the output stage.

The CH2 was developed to filter the signals generated by the impact with a sphere in free-fall. The default attenuation is set 1:1, suitable for processing typical signals of a high sensitivity sensor, such as PI, and with impact characteristics, such as the case reported in the "e" column of Table 2.

In the case of impacts with greater energy, it is sufficient to set the attenuation to an adequate value.

The signal is then filtered analogically through the filter already described in paragraph 1.6, reaching a peak voltage of about 210 mVpp with a gain of 9 v/v, to have amplitudes such as to be able to exploit most of the dynamics of the ADC.

On this channel, it is therefore possible to acquire high-frequency signals, generated by low energy impacts, which contain both the S_0 component and the A_0 component.

Channel CH3 has been developed to process the signals generated by the electromechanical impactor. The default attenuation is set 1:1. Always considering the same distance of 10 cm from the point of impact, the signal acquired is coupled through a low noise impedance buffer adapter and then amplified with 13 v/v gain.

This signal, after high pass filtering, has a lower amplitude and needs further amplification by a factor of 16, so that the processed signals have an output dynamics of ±800 mV. In this case, the output stage amplifier can further amplify the signal to take advantage of all the dynamics of the ADC. The signals processed in this way have the high-frequency A_0 component. The S_0 component, which we remember according to the impact speed, is difficult to distinguish from the noise.

The second function of channel CH3 is the detection of only the S_0 component generated by the sphere impacts: in this case the A_0 component will be saturated and clipped at the ADC input, but this is not a problem because the informative contribution for the triangulation algorithms belongs to the earlier S_0.

The choice of the operational amplifiers to be used in this chain depends on power consumption requirements. In a main power sensor network, the power supply has fewer constraints, while for an autonomous node battery operation, the choice of a low voltage op-amp is mandatory. However, the validity of the AFE architecture presented in this work remains valid. In our case, the available power supply was $+/3.3$ V or $+/-5$ V, we then decided on the larger one. The LF347 has a low consumption rate, introduces a minimum amount of noise in the signal bandwidth, and has a high slew rate: its unity gain band is adequate for the observed signals. It is therefore suitable for the buffer function in this application.

The LM6172 is also a low consumption op-amp, and its large gain-bandwidth product allows amplification and active filtering of signals; moreover, it has a high output current and is therefore suitable for driving subsequent stages.

4. Design and Realization of a Versatile Analog Front-End Module

Once the correct operation of the multichannel front-end was found in a through-hole prototype, small surface-mount (SMD) multichannel front-end were created, including connectors for the input and output signals (see Figure 12). A female jack type female connector was chosen for the input. A second input has also been inserted, with a micro-USB connection as an alternative to the jack connection. An SMA connector was used for the output of the front-end board for connection to the multi-channel electronic platform. In Figure 12, the side view of a module is illustrated: a shield has been adopted to limit the electro-magnetic-interference (EMI) with other mixed-signal modules in proximity and the USB connector as an alternative connector with respect to the dual in-line connector to the backplane. In this way, the module can also be used as a stand-alone.
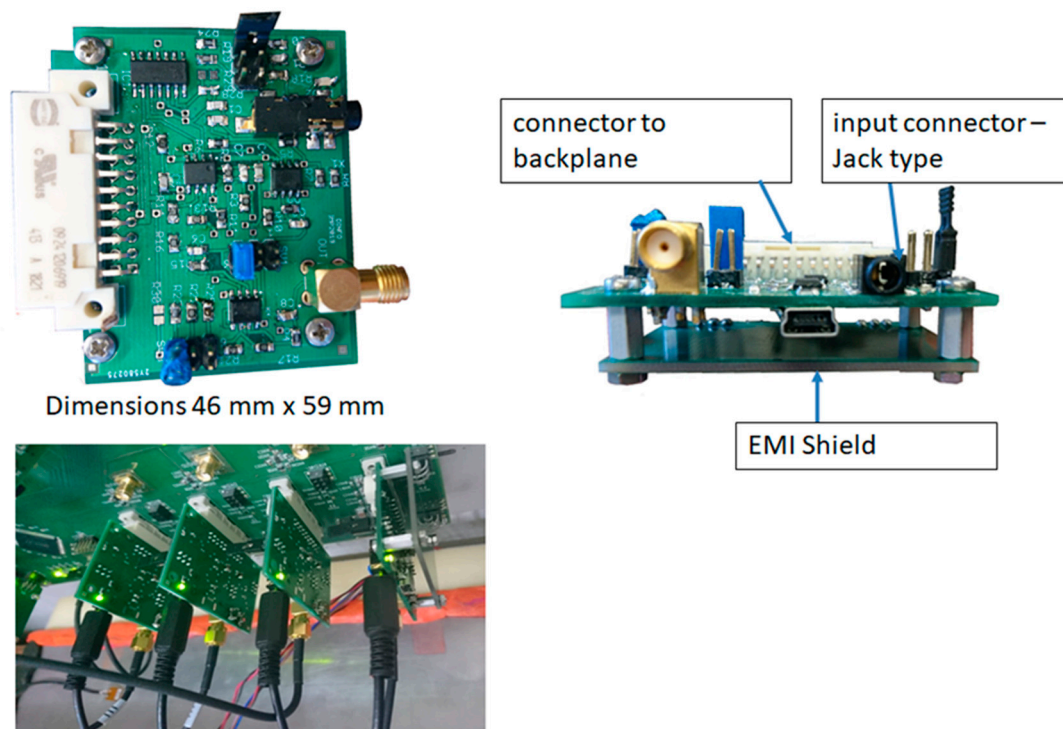
Figure 12. (**Top**) The board with the analog electronic front end. (**Bottom**) Modular installation boards on the backplane of the real-time electronic platform for SHM.

Design and Realization of a Versatile Analog Front-End Modules

The frequency-domain responses of two modular SMD boards have been measured and compared with simulation. The characterization is important for the assessment of reproducibility among different modules and the possible presence of positive feedback leading to poor circuit stability and frequency response peaking.

Reported in Table 3 is the characterization for the three channels (CH1, CH2, CH3). The characteristics of the prototypes have been measured and averaged among the 16 modules realized for the multichannel platform. The values are in good agreement with simulations, considering the error propagation of the SMD components tolerances (5%) and the filter circuit topology.

Table 3. Characterization of gain and frequency response of the three channels.

Channel #	Gain		Bandwidth (−3dB)	
	Simulated	Measured	Simulated	Measured
CH 1	−0.4 dB	−1 dB	0–500 kHz	0–400 kHz
CH 2	30 dB	30 dB	200–700 kHz	210–600 kHz
CH 3	57 dB	56 dB	200–550 kHz	200–550 kHz

It can be concluded that the 16 multifunctional front ends have comparable transfer functions for the 3 channels, so the acquired signals are conditioned in the same way.

The propagation times within the channels were also measured (see Table 4). To measure the delay times, a sinusoidal cycle burst with a chosen frequency Fi (i = 1,2,3) within the band of interest was used. The travel times recorded on the CH1 are constant as the frequency varies, consistent for the two prototypes. The differences recorded are irrelevant for the purpose of calculating the DToA, which have quantities of the order of microseconds. The same considerations apply to CH2 and CH3. Front-end showing the same signal delays do not have a significant influence on DToAs.

Table 4. Delay times for the three channels of the AFE.

	F_1	F_2	F_3
Freq (kHz)	1	80	200
CH1			
Front-end #1	470 ns	468 ns	456 ns
Front-end #2	472 ns	470 ns	462 ns
CH2			
Front-end #1	478 ns	450 ns	320 ns
Front-end #2	478 ns	448 ns	322 ns
CH3			
Front-end #1	498 ns	420 ns	320 ns
Front-end #2	496 ns	423 ns	322 ns

The output noise of the CH2 and CH3 channels was measured because they are the channels dedicated to the conditioning of low amplitude signals. For this measurement, an impedance of 50 Ω was placed at the input, and the Vrms output from the module was measured using the Tektronix TDS3012B digital oscilloscope with a band limited to 20 MHz. The SNR was evaluated by using a one cycle burst sinusoidal signal at the central band frequency of the channel under examination, with an amplitude of 10 mV, then the rms value of the output signals is recorded (see Table 5). Values exceeding 72 dB allow the processing of small impact signals and justify the use of ADC with 12-bit resolution.

Table 5. Signal-to-noise ratio in decibels of the module for the selection of CH2 and CH3.

	SNR Front-End #1	SNR Front-End #2
CH2	72 dB	72 dB
CH3	76 dB	76 dB

The power consumption estimation is important for the dimensioning of the power management of the sensor node (see Figure 1). The analog front-end is powered with a dual ± 5 V power supply and absorbs 20 mA of current, therefore consumption is 200 mW. Considering that the development platform can host up to 16 modules, the total power is 3.2 W. This value certainly requires management by means of high-efficiency and low noise switching DC/DC converters to avoid problems of thermal dissipation and available energy dissipation.

For continuous monitoring in sensor nodes, the use of AFE activation techniques in the presence of an event detection has been proposed in [35]. In the interest of developing an embedded system, it is necessary to select integrated devices that operate with a lower power supply (e.g., single supply 3.3 V).

5. Experimental Results

To validate the whole system, we organized an experiment with four PI sensors installed on the aluminum plate in different positions, and an impact in a known position was carried out with a free-falling sphere with an impact final velocity of 1.2 m/s. The four AFE modules were programmed for CH3 and no attenuation at the input.

In this way, the maximum amplification was exploited for the early detection of the S_0 mode signal and the determination of the DToAs by first peak detection with a simple threshold method. For comparison, the same experiment was repeated by using the CH2 for the acquisition of A_0 mode and subsequent DToA processing.

The experiment is carried out with 4 + 4 PI sensors connected to programmable AFE modules and installed on the aluminum plate. Colored play dough was placed at the edges of the plate to attenuate reflections from boundaries.

The configuration for the experiment is done by comparing the results obtained by one group of four sensors and processing the A_0 mode and another group of sensors for

processing the S_0 mode; the corresponding group velocities are 1450 m/s and 5500 m/s, respectively. For the A_0 mode, the electromechanical impactor (see Figure 13) was used, while for the S_0 mode, the free-falling mass impactor in the same point was used. The estimated DToAs and the corresponding distances D_{xi-j} are reported in Table 6. The resulting analysis is interesting, as it reveals the advantages of using a simple threshold method on the detectable S_0, which is most accurate for the application of triangulation methods based on distance estimations. The error is always less than 5 mm, which is lower than the S0 mode central wavelength equal to VgroupS0/fcut-off = 5500/270000 = 20 mm.
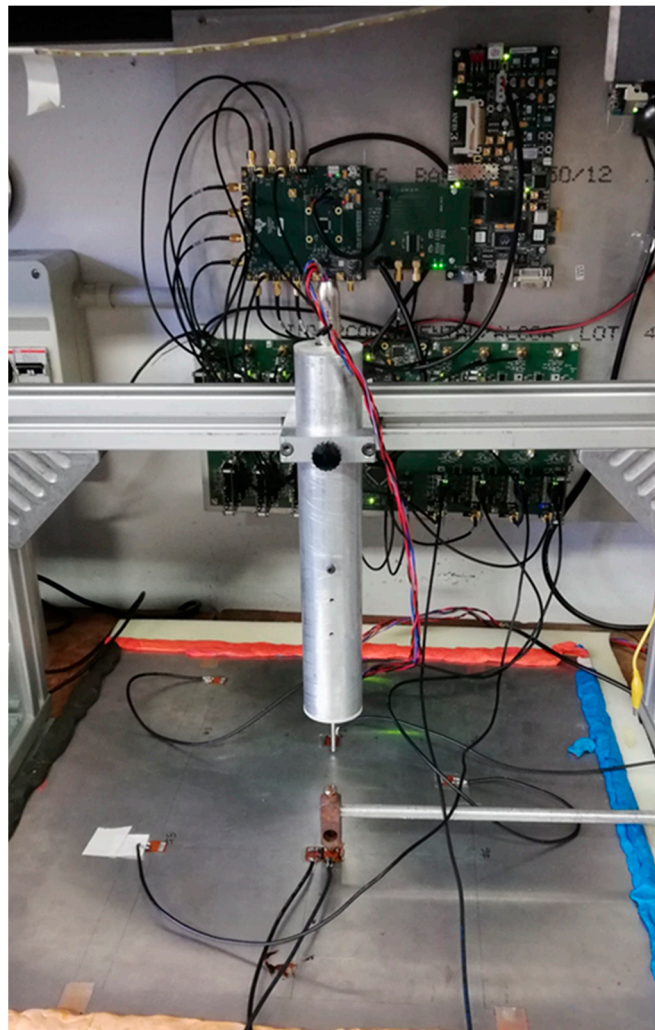
Figure 13. The experimental setup for impact continuous monitoring by a 16-module electronic platform. The picture shows the two impactors: the electromechanical programmable impactor with a thin steel bar integrated into the vertical cylindrical case (shown in the center), and a free-fall mass mounted on an arm with 1 angular degree of freedom (shown on the bottom-right).

The design and characterization of the three channels present in each module demonstrate the advantage of customizing the AFE to obtain the best performance in an impact monitoring system that can be implemented with different sensors. Furthermore, the proposed signal chain is easy to implement even in a more compact and replicable technology, such as ASIC or custom chip. The advantages of the integrated electronic design for the sensor node are well described in the articles by Tang et al. [52,53]. To reduce the footprint of a custom IC, it is necessary to keep in mind the difficulty of integrating the passive components used in active filters; in the project presented here, capacitor values lower than 5nF have been adopted.

Table 6. DToAs and distance estimation with A_0 and S_0 mode signals.

	Data from S_0 Mode – AFE CH3 Selected – Vgroup_S_0 = 5550 m/s					Data from A_0 Mode – AFE CH2 Selected – Vgroup_A_0 = 1450 m/s			
Path	DTOA (μs)	Calculated Distance (mm)	Actual Distance (mm)	Error (mm)	Path	DTOA (μs)	Calculated Distance (mm)	Actual Distance (mm)	Error (mm)
$D_{x1\text{-}2}$	9.20	50.6	50.1	−0.5	$D_{x1\text{-}2}$	13.54	19.6	27.9	8.3
$D_{x1\text{-}3}$	19.90	109.5	105.1	−4.3	$D_{x1\text{-}3}$	43.12	62.5	105.1	42.6
$D_{x1\text{-}4}$	24.00	132.0	135.5	3.5	$D_{x1\text{-}4}$	59.62	86.5	135.5	49.1
$D_{x2\text{-}3}$	10.70	58.9	55.0	−3.8	$D_{x2\text{-}3}$	29.59	42.9	77.2	34.3
$D_{x2\text{-}4}$	15.40	84.7	85.3	0.6	$D_{x2\text{-}4}$	46.08	66.8	107.5	40.7
$D_{x3\text{-}4}$	4.70	25.9	30.3	4.5	$D_{x3\text{-}4}$	16.50	23.9	30.3	6.4

6. Conclusions

In this paper, we have investigated the design of a versatile analog front-end for interfacing piezoelectric sensors for capturing ultrasonic guided modes generated by impacts on a mechanical structure. This type of waves, called Lamb waves, are multimodal, dispersive and have frequency-dependent attenuation.

We have considered all these physical factors to create a set of quantitative data for deciding the electronic interface requirements. The paper describes this preliminary step, providing the reader with the ability to reproduce the same analysis for other electronic interface design devoted to SHM applications.

One of the main objectives was to separate the signals arising from the A_0 and S_0 Lamb wave modes. This is achieved by the design of three different chains with different gain and frequency response, and they are:

(1) Chain 1—for impact detection and energy determination with no gain by low frequency (up to 20 kHz) spectral content of A_0 mode.
(2) Chain 2—for extraction of high-frequency components (higher than 220 kHz) of the A0 mode for low impact velocity with moderate gain (9 v/v).
(3) Chain 3—for extraction of high-frequency components (higher than 220 kHz) of the S0 mode for low and high impact velocity with large gain (208 v/v).
(4) A programmable input selector for accommodating the sensitivity of different piezoelectric sensors sensitivity and avoid saturation of the electronics for high energy impacts.
(5) An output filter at 800 kHz for limiting the in-band noise.

Thanks to the versatility of this analog chain, each module can host different sensors and has different functionality. This is an advantage of designing an SHM sensor network where not all nodes have the same purpose. Moreover, when these modules are integrated with a multichannel acquisition platform, the system can provide in real-time several characteristics of impact events. This strategy alleviates the computational and digital data handling requirements of the electronics that can be embedded in a single node.

The signal-to-noise ratio obtained exceeds 72 dB, and power consumption and time delays of electronics (always less than 500 ns) are replicable on different units.

The benefit of this solution for the electronic interface is demonstrated with experimental tests on a network of four piezoelectric sensors of patch type installed on an aluminum plate.

The differential arrival times (DToAs) of the first arrival signal are obtained by the S_0 mode signals by a simple thresholding method. The errors on distance evaluation are always less than 5 mm over distances from the impact point of about 200 mm and an S_0 mode wavelength of 20 mm. This good performance for DToA estimation is then exploited on post-processing for localization of the impact point by common triangulation algorithms. The threshold method is simple to be implemented in real-time for continuous monitoring and does not require much power being based on a comparator stage. Each module can be used and programmed also in a stand-alone mode.

In summary, the AFE modules installed on a multichannel modular platform can be used to arrange optimal sensor layout for continuous monitoring by deploying different types of sensors, and they can be individually programmed for specific analog signal pre-processing tasks (impact detection, impact energy, DToA).

References

1. Ferin, G.; Muralidharan, Y.; Mesbah, N.; Chatain, P.; Bantignies, C.; le Khanh, H.; Flesch, E. An Nguyen-Dinh Smart Autonomous Wireless Acoustic Sensors for Aeronautical SHM Applications. In Proceedings of the 2015 IEEE International Ultrasonics Symposium (IUS), Taipei, Taiwan, 21–25 October 2015; IEEE: Taipei, Taiwan, 2015; pp. 1–4.
2. Scheerer, M.; Lager, D. Development and Testing of A Hybride Active—Passive Acoustic Shm System for Impact Damage Detection in Honeycomb Aircraft Structures. In Proceedings of the 19th International Conference On Composite Materials, Montreal, QC, Canada, 28 July–2 August 2013.
3. Bao, Y.; Chen, Z.; Wei, S.; Xu, Y.; Tang, Z.; Li, H. The State of the Art of Data Science and Engineering in Structural Health Monitoring. *Engineering* **2019**, *5*, 234–242. [CrossRef]
4. Ciang, C.C.; Lee, J.-R.; Bang, H.-J. Structural Health Monitoring for a Wind Turbine System: A Review of Damage Detection Methods. *Meas. Sci. Technol.* **2008**, *19*, 122001. [CrossRef]
5. Boubenia, R.; Bourbon, G.; le Moal, P.; Joseph, E.; Ramasso, E.; Placet, V. Acoustic Emission Sensing Using MEMS for Structural Health Monitoring: Demonstration of a Newly Designed Capacitive Micro Machined Ultrasonic Transducer. In Proceedings of the 12th International Workshop on Structural Health Monitoring, Stanford, CA, USA, 10–12 September 2019.
6. Farrar, C.R.; Worden, K. An Introduction to Structural Health Monitoring. In *New Trends in Vibration Based Structural Health Monitoring*; Deraemaeker, A., Worden, K., Eds.; CISM International Centre for Mechanical Sciences; Springer: Vienna, Austria, 2010; Volume 520, pp. 1–17. ISBN 978-3-7091-0398-2.
7. Ju, Z.; Li, F.; Janapati, V.; Chung, H.; Yadav, S.; Cheung, C. *Sensor Network Design Technique for Monitoring Railroad Structures*. In Proceedings of the 1st International Workshop on Structural Health Monitoring for Railway System, Qingdao, China, 12–14 October 2016.
8. Boukabache, H.; Escriba, C.; Fourniols, J.-Y. Toward Smart Aerospace Structures: Design of a Piezoelectric Sensor and Its Analog Interface for Flaw Detection. *Sensors* **2014**, *14*, 20543–20561. [CrossRef] [PubMed]
9. De Simone, M.E.; Ciampa, F.; Boccardi, S.; Meo, M. Impact Source Localisation in Aerospace Composite Structures. *Smart Mater. Struct.* **2017**, *26*, 125026. [CrossRef]
10. Park, G.; Farinholt, K.M.; Farrar, C.R.; Rosing, T.; Todd, M.D. Powering Wireless SHM Sensor Nodes through Energy Harvesting. In *Energy Harvesting Technologies*; Priya, S., Inman, D.J., Eds.; Springer: Boston, MA, USA, 2009; pp. 493–506. ISBN 978-0-387-76463-4.
11. Mitra, M.; Gopalakrishnan, S. Guided Wave Based Structural Health Monitoring: A Review. *Smart Mater. Struct.* **2016**, *25*, 053001. [CrossRef]
12. Aranguren, G.; Monje, P.M.; Cokonaj, V.; Barrera, E.; Ruiz, M. Ultrasonic Wave-Based Structural Health Monitoring Embedded Instrument. *Rev. Sci. Instrum.* **2013**, *84*, 125106. [CrossRef]
13. Gao, F.; Zeng, L.; Lin, J.; Shao, Y. Damage Assessment in Composite Laminates via Broadband Lamb Wave. *Ultrasonics* **2018**, *86*, 49–58. [CrossRef] [PubMed]
14. Ewald, V.; Groves, R.; Benedictus, R. Transducer Placement Option of Lamb Wave SHM System for Hotspot Damage Monitoring. *Aerospace* **2018**, *5*, 39. [CrossRef]
15. Bulletti, A.; Capineri, L. Interdigital Piezopolymer Transducers for Time of Flight Measurements with Ultrasonic Lamb Waves on Carbon-Epoxy Composites under Pure Bending Stress. *J. Sens.* **2015**, *2015*, 1–11. [CrossRef]
16. Kirkby, E.; de Oliveira, R.; Michaud, V.; Månson, J.A. Impact Localisation with FBG for a Self-Healing Carbon Fibre Composite Structure. *Compos. Struct.* **2011**, *94*, 8–14. [CrossRef]
17. Boffa, N.D.; Monaco, E.; Ricci, F.; Memmolo, V. Hybrid Structural Health Monitoring on Composite Plates with Embedded and Secondary Bonded Fiber Bragg Gratings Arrays and Piezoelectric Patches. In Proceedings of the 11th International Symposium NDT in Aerospace (AeroNDT 2019), Paris-Saclay, France, 13–15 November 2019.
18. Datta, A.; Augustin, M.J.; Gupta, N.; Viswamurthy, S.R.; Gaddikeri, K.M.; Sundaram, R. Impact Localization and Severity Estimation on Composite Structure Using Fiber Bragg Grating Sensors by Least Square Support Vector Regression. *IEEE Sens. J.* **2019**, *19*, 4463–4470. [CrossRef]

19. Shin, C.S.; Chen, B.L. An Impact Source Locating System Using Fiber Bragg Grating Rosette Array. In Proceedings of the Third International Conference on Smart Materials and Nanotechnology in Engineering, Shenzhen, China, 2 April 2012; p. 84091B.

20. Farrar, C.R.; Park, G.; Todd, M.D. Sensing Network Paradigms for Structural Health Monitoring. In *New Developments in Sensing Technology for Structural Health Monitoring*; Mukhopadhyay, S.C., Ed.; Lecture Notes in Electrical Engineering; Springer: Berlin/Heidelberg, Germany, 2011; Volume 96, pp. 137–157. ISBN 978-3-642-21098-3.

21. Giannì, C.; Balsi, M.; Esposito, S.; Ciampa, F. Low-power Global Navigation Satellite System-enabled Wireless Sensor Network for Acoustic Emission Localisation in Aerospace Components. *Struct. Control. Health Monit.* **2020**, *27*. [CrossRef]

22. Jeongyeup, P.; Chintalapudi, K.; Govindan, R.; Caffrey, J.; Masri, S. A Wireless Sensor Network for Structural Health Monitoring: Performance and Experience. In Proceedings of the Second IEEE Workshop on Embedded Networked Sensors, Sydney, Australia, 31 May 2005; EmNetS-II. IEEE: Sydney, Australia, 2005; pp. 1–10.

23. Bulletti, A.; Giannelli, P.; Calzolai, M.; Capineri, L. An Integrated Acousto/Ultrasonic Structural Health Monitoring System for Composite Pressure Vessels. *IEEE Trans. Ultrason. Ferroelectr. Freq. Control.* **2016**, *63*, 864–873. [CrossRef]

24. Capineri, L.; Bulletti, A.; Calzolai, M.; Francesconi, D. A Real-Time Electronic System for Automated Impact Detection on Aircraft Structures Using Piezoelectric Transducers. *Procedia Eng.* **2014**, *87*, 1243–1246. [CrossRef]

25. Marino-Merlo, E.; Bulletti, A.; Giannelli, P.; Calzolai, M.; Capineri, L. Analysis of Errors in the Estimation of Impact Positions in Plate-Like Structure through the Triangulation Formula by Piezoelectric Sensors Monitoring. *Sensors* **2018**, *18*, 3426. [CrossRef] [PubMed]

26. Aly, K.; Bradford, P.D. Real-Time Impact Damage Sensing and Localization in Composites through Embedded Aligned Carbon Nanotube Sheets. *Compos. Part B Eng.* **2019**, *162*, 522–531. [CrossRef]

27. Ciampa, F.; Meo, M. A New Algorithm for Acoustic Emission Localization and Flexural Group Velocity Determination in Anisotropic Structures. *Compos. Part Appl. Sci. Manuf.* **2010**, *41*, 1777–1786. [CrossRef]

28. Ebrahimkhanlou, A.; Salamone, S. Acoustic Emission Source Localization in Thin Metallic Plates: A Single-Sensor Approach Based on Multimodal Edge Reflections. *Ultrasonics* **2017**, *78*, 134–145. [CrossRef] [PubMed]

29. Rose, J. Ultrasonic Guided Waves in Structural Health Monitoring. *Key Eng. Mater.* **2004**, *270–273*, 14–21. [CrossRef]

30. Ono, K. Review on Structural Health Evaluation with Acoustic Emission. *Appl. Sci.* **2018**, *8*, 958. [CrossRef]

31. Beattie, A. *Acoustic Emission Non-Destructive Testing of Structures Using Source Location Techniques*; Sandia National Laboratories: Albaquerque, NM, USA, 2013.

32. Qing, X.; Li, W.; Wang, Y.; Sun, H. Piezoelectric Transducer-Based Structural Health Monitoring for Aircraft Applications. *Sensors* **2019**, *19*, 545. [CrossRef]

33. Schubert, L.; Frankenstein, B.; Reppe, G. Match-X Based Microsystem for Structural Health Monitoring. In Proceedings of the 1st Electronic Systemintegration Technology Conference, Dresden, Germany, 5–7 September 2006; IEEE: Dresden, Germany, 2006; pp. 635–641.

34. Fu, H.; Sharif Khodaei, Z.; Aliabadi, M.H.F. An Event-Triggered Energy-Efficient Wireless Structural Health Monitoring System for Impact Detection in Composite Airframes. *IEEE Internet Things J.* **2019**, *6*, 1183–1192. [CrossRef]

35. Overly, T.G.S.; Park, G.; Farinholt, K.M.; Farrar, C.R. Development of an Extremely Compact Impedance-Based Wireless Sensing Device. *Smart Mater. Struct.* **2008**, *17*, 065011. [CrossRef]

36. Hertz, H. Ueber Die Berührung Fester Elastischer Körper. *J. Für Reine Angew. Math. Crelles J.* **1882**, *1882*, 156–171. [CrossRef]

37. Yang, J.C.S.; Chun, D.S.; MD, N.O.L.W.O. *Application of the Hertz Contact Law to Problems of Impact in Plates*; Defense Technical Information Center: Fort Belvoir, VA, USA, 1969.

38. Staszewski, W.J.; Mahzan, S.; Traynor, R. Health Monitoring of Aerospace Composite Structures—Active and Passive Approach. *Compos. Sci. Technol.* **2009**, *69*, 1678–1685. [CrossRef]

39. Bernard, A.; Lowe, M.J.S.; Deschamps, M. Guided Waves Energy Velocity in Absorbing and Non-Absorbing Plates. *J. Acoust. Soc. Am.* **2001**, *110*, 186–196. [CrossRef]

40. Degertakin, F.L.; Khuri-Yakub, B. Lamb Wave Excitation by Hertzian Contacts with Applications in NDE. *IEEE Trans. Ultrason. Ferroelectr. Freq. Control.* **1997**, *44*, 769–779. [CrossRef]

41. Pieczonka, L.; Aymerich, F.; Staszewski, W.J. Impact Damage Detection in Light Composite Sandwich Panels. *Procedia Eng.* **2014**, *88*, 216–221. [CrossRef]

42. Gorman, M.R.; Humes, D.H.; June, R.; Prosser, W.H.; Prosser, W.H. Acoustic Emission Signals in Thin Plates Produced by Impact Damage. *J. Acoust. Emiss.* **1999**, *17*, 29–36.

43. Miniaci, M.; Mazzotti, M.; Radzieński, M.; Kudela, P.; Kherraz, N.; Bosia, F.; Pugno, N.M.; Ostachowicz, W. Application of a Laser-Based Time Reversal Algorithm for Impact Localization in a Stiffened Aluminum Plate. *Front. Mater.* **2019**, *6*, 30. [CrossRef]

44. Nicassio, F.; Carrino, S.; Scarselli, G. Non-Linear Lamb Waves for Locating Defects in Single-Lap Joints. *Front. Built Environ.* **2020**, *6*, 45. [CrossRef]

45. Mevissen, F.; Meo, M. A Nonlinear Ultrasonic Modulation Method for Crack Detection in Turbine Blades. *Aerospace* **2020**, *7*, 72. [CrossRef]

46. Ziola, S.M.; Gorman, M.R. Source Location in Thin Plates Using Cross-correlation. *J. Acoust. Soc. Am.* **1991**, *90*, 2551–2556. [CrossRef]

47. Smithard, J.; Rajic, N.; van der Velden, S.; Norman, P.; Rosalie, C.; Galea, S.; Mei, H.; Lin, B.; Giurgiutiu, V. An Advanced Multi-Sensor Acousto-Ultrasonic Structural Health Monitoring System: Development and Aerospace Demonstration. *Materials* **2017**, *10*, 832. [CrossRef]

48. Lee, B.C.; Staszewski, W.J. Modelling of Lamb Waves for Damage Detection in Metallic Structures: Part I. Wave Propagation. *Smart Mater. Struct.* **2003**, *12*, 804–814. [CrossRef]

49. Ross, R. Structural Health Monitoring and Impact Detection Using Neural Networks for Damage Characterization. In Proceedings of the 47th AIAA/ASME/ASCE/AHS/ASC Structures, Structured Dynamics, and Materials Conference, Newport, RI, USA, 1–4 May 2006; Volume 9.

50. Tobias, A. Acoustic-Emission Source Location in Two Dimensions by an Array of Three Sensors. *Non-Destr. Test.* **1976**, *9*, 9–12. [CrossRef]

51. Lamb, H. On Waves in an Elastic Plate. *Proc. R. Soc. Lond. Ser. Contain. Pap. Math. Phys. Character* **1917**, *93*, 114–128.

52. Tang, X.; Zhao, H.; Mandal, S. A Highly-Integrated CMOS Transceiver for Active Structural Health Monitoring. In Proceedings of the 2016 IEEE National Aerospace and Electronics Conference (NAECON) and Ohio Innovation Summit (OIS), Dayton, OH, USA, 25–29 July 2016; IEEE: Dayton, OH, USA, 2016; pp. 133–138.

53. Tang, X.; Zhao, H.; Mandal, S. A Programmable CMOS Transceiver for Structural Health Monitoring. In Proceedings of the 2018 IEEE Custom Integrated Circuits Conference (CICC), San Diego, CA, USA, 8–11 April 2018; IEEE: San Diego, CA, USA, 2018; pp. 1–4.